# Magnetic behavior of Fe-doped zirconia studied by synchrotron radiation measurements and first-principles simulations

R. Ciprian,[1] A. Lamperti,[2] L. Capasso,[1] F. Motti,[3,4] E. Cianci,[2] E. Weschke,[5] P. Torelli,[3] and A. Debernardi[2,*]

[1]*Elettra Sincrotrone di Trieste, s.s. 14, km 163.5, 34149 Basovizza, Trieste, Italy*

[2]*CNR-IMM, Agrate Unit, via C. Olivetti 2, 20864 Agrate Brianza (MB), Italy*

[3]*Istituto Officina dei Materiali (IOM)-CNR, Laboratorio TASC, Area Science Park, S.S. 14 km 163.5, Trieste I-34149, Italy*

[4]*Dipartimento di Fisica, Universitá degli Studi di Milano, via Celoria 16, I-20133 Milano, Italy*

[5]*Helmholtz-Zentrum Berlin für Materialien und Energie, Albert-Einstein-Strasse 15, 12489 Berlin, Germany*

(Received 27 May 2019; revised manuscript received 27 March 2020; accepted 21 April 2020; published 27 May 2020)

Exploiting first-principles simulations and x-ray absorption near edge spectroscopy (XANES) in high magnetic fields, we investigated the magnetic properties of thin films of zirconia doped with Fe impurities. In our $Zr_{1-x}Fe_xO_{2-y}$ samples, grown by atomic layer deposition (ALD), the Fe dopants are uniformly distributed, ranging from diluted ($x \simeq 2$–$3\%$) up to high ($x \simeq 25\%$) atomic concentration. By x-ray magnetic circular dichroism (XMCD), we carefully analyzed, for samples having different Fe concentration, the magnetic moments as a function of temperature, in the range from 5 K up to 150 K, studying the best dopant concentration range maximizing the magnetic signal. Surprisingly, the iron magnetic moment measured for diluted concentrations degrades as the concentration of magnetic dopant increases. On the basis of *ab initio* simulations, we propose that the microscopic mechanisms responsible for the peculiar magnetic properties of this compound can be explained by oxygen-mediated superexchange mechanism between the Fe dopants producing, at high dopant concentration, an antiferromagnetic coupling between two Fe atoms. We identify and discuss the role of O vacancies to control such microscopic mechanisms.

DOI: 10.1103/PhysRevMaterials.4.054417

## I. INTRODUCTION

The synthesis of magnetic semiconductors promises the realization of innovative devices in which the spin of the carriers is exploited as a further degree of freedom in addition to their charge, allowing efficient (and scalable) data storage and transfer [1]. In this context, the availability of room-temperature magnetic semiconductors strongly dictates the possibility to realize commercial spintronic devices that will revolutionize the semiconductor industry in the following years. In the search for room-temperature magnetic semiconductors a significant amount of effort has been dedicated towards the study of diluted magnetic oxides (DMO) [2], i.e., compounds with diluted concentration of magnetic impurities uniformly and randomly distributed in the oxide matrix. In particular, the identification of the microscopic mechanisms responsible for magnetic properties in DMO is of paramount importance because it will pivot the research to novel forthcoming spintronic devices.

Since the prediction that Mn-doped zirconia can support room-temperature ferromagnetism [3], the attention of material scientists has been focused on magnetically doped zirconia [4–7] and hafnia [8,9], two similar oxides already extensively studied by the semiconductor industry for their high-dielectric properties [10]. Several works attempted to determine the magnetic nature of transition metal doped zirconia (or hafnia). However, the experimental studies produced contrasting results, suggesting the presence [11–14] or the absence [15] of room-temperature ferromagnetism. Furthermore, the magnetic nature of these compounds is still debated (i.e., ferromagnetic (FM) [16], antiferromagnetic (AFM) [17], paramagnetic (PM) [18], or super-PM (SPM)). During the past years, the interpretation of results in the field of diluted magnetic oxides was hindered by some reports about ferromagnetic behavior at room temperature that lately turned out to be originating from spurious signals and artifacts in the measurements (see, for example, Ref. [19] for a more detailed discussion of this issue).

To avoid possible artifacts encountered with superconducting quantum interference device vibrating sample magnetometry (SQUID-VSM), we employed state-of-the-art x-ray magnetic circular dichroism (XMCD) to investigate the temperature dependence of the magnetic properties of Fe-doped zirconia, for different dopant concentrations. Our measurements show that at low temperature and diluted concentrations, a magnetic field can induce a big (up to $1.8\,\mu_B$) magnetic moment on the Fe ion while the magnetic moment decreases as the Fe concentration increases. This surprising behavior is explained by *ab initio* simulations, in terms of superexchange interactions, which, for peculiar Fe configurations at diluted doping, can cause a FM coupling on a finite portion of the crystal, thus producing the detected magnetic moment. At variance, at high doping regime, the

*Corresponding author: alberto.debernardi@mdm.imm.cnr.it

 

superexchange mechanism produces an AFM coupling between two neighbor Fe dopants substitutional to Zr, mediated by an O in a "bridge" position between the two magnetic impurities.

## II. EXPERIMENTAL RESULTS

The samples consist of thin film of Fe-doped fluorite zirconia grown by atomic layer deposition. Fe is uniformly distributed at substitutional Zr sites in the zirconia matrix, as demonstrated in previous publications [20–22]. For overall charge neutrality, the Fe doping induces the formation of O vacancies ($V_O$), thus forming the compound $Zr_{1-x}Fe_xO_{2-y}$, with $y$ very close to $x/2$ [20], i.e., one $V_O$ every two Fe ($y = x/2$) corresponding to the case with $Fe^{3+}$ oxidation state. In the opposite limiting case of $Fe^{2+}$, $y$ is expected to be close to $x$, while intermediate values of $y$ correspond to different $Fe^{3+}/Fe^{2+}$ ratios. The samples were measured at the BESSY synchrotron radiation facility in Berlin, Germany, by x-ray absorption near-edge spectroscopy (XANES) and x-ray magnetic circular dichroism (XMCD) at Fe $L_{2,3}$ and O $K$ edges. The elemental sensitivity of XMCD ensures that the actual magnetic signal is coming from the elements inside the sample, and not from spurious sources such as impurities or the sample holder. Furthermore, elemental sensitivity is useful in the debate around the origin of magnetism in diluted oxides. Indeed it was also proposed that the magnetic moment may reside not only in the dopants [19]. Details of the sample characterization and measurement conditions are reported in Appendixes A and B, respectively.

Figures 1(a) and 1(b) show the XANES spectra acquired at O $K$ and Fe $L_{2,3}$ edges for the $ZrO_2$ samples doped with different concentrations of Fe at 5 K. The O $K$ edge spectra [Fig. 1(a)] can be subdivided into three main regions. Region I, for energies lower than 531 eV, is characterized by a low intensity peak ascribed to O 2$p$ states hybridized with Fe 3$d$ states [23,24], in particular it originates from O atoms with a Fe atom in their first coordination shell [25]. Region II, corresponding to energies in the range from 531 to 541 eV, shows spectral features mainly due to the transition from the O 1$s$ and the O 2$p$ states hybridized with the Zr 4$d$ states [26,27]. Region III, above 541 eV, shows features due to O 2$p$ states mixed with Zr 5$s$ states. The well-resolved shape of the edge-peak (∼537 eV) indicates that the samples are crystalline, while the increase in broadness as a function of the dopant concentration is related to the chemical disorder produced by Fe substitutional impurities randomly distributed at the Zr sublattice sites [25,27,28].

The Fe $L_{2,3}$ spectra [Fig. 1(b), see also Fig. 2(a)] are due to transitions from 2$p$ core level into empty 3$d$ states of Fe in the presence of a crystal field [29]. The presence of localized states both at $L_3$ and $L_2$ reveals a mixture of $Fe^{2+}$ and $Fe^{3+}$ states (see, for example, Refs. [30,31]). This can be stated by a comparison with crystal-field multiplet calculations, which predict a shift in the main peak for different valence states of Fe (regardless of the crystal field symmetry) [32]. Unfortunately, the energy separation of the main peak between $Fe^{3+}$ and $Fe^{2+}$ closely matches the crystal field splitting for $Fe_2O_3$, so the presence of such a phase on the local scale cannot be ruled out completely.

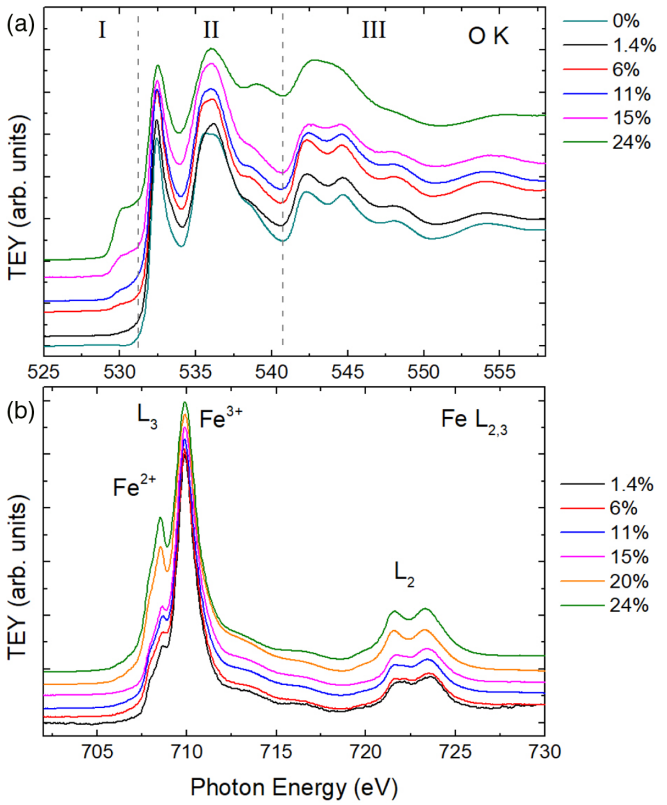


FIG. 1. XANES spectra acquired in Total Electron Yield mode at $T = 5$ K and at the (a) O $K$ and (b) Fe $L_{2,3}$ edges of the $ZrO_2$ samples doped with different concentrations of Fe.

Following our main interpretation, for Fe concentration <15 at.% the 3+ valence of Fe is the largely predominant oxidation state [Fig. 3(a)], however, for higher dopant concentration, the $Fe^{3+}/Fe^{2+}$ ratio drops. Indeed, the pre-edge peak (∼708.7 eV) increases in sharpness and intensity [Fig. 1(b)] indicating a significant increases in the amount of $Fe^{2+}$. Since Fe replaces a $Zr^{4+}$ atom, the increase in $Fe^{2+}$ sites can be related to a significant increase in the amount of O vacancies (i.e., in $Zr_{1-x}Fe_xO_{2-y}$, $y$ grows from $x/2$ towards $x$). From the O $K$ edge spectra, the drop of the $Fe^{3+}/Fe^{2+}$ ratio happens to be correlated by a steep increase in the intensity of the O pre-edge peak at about 530 eV [see Fig. 1(a) and Fig. 3(a)] and to a decrease in intensity of the peak at 537 eV [25].

No magnetic contrast was found at the O $K$ and Zr $L_{2,3}$ edges, while a very strong signal was found at the Fe $L_{2,3}$ edges. A representative example is shown in Fig. 2. In particular, the highest XMCD signal was found for the lowest dopant concentration, and it decreases monotonically for higher content of Fe. At 24 at.% doping, it is almost zero [Fig. 3(b)].

This signal reduction is in agreement with the increase in the amount of $Fe^{2+}$ (having a smaller magnetic moment than $Fe^{3+}$) in the highly doped samples. However, the observed decrease of the XMCD signal cannot be explained only by the difference in the $Fe^{3+}/Fe^{2+}$ ratio. Supposing that the magnetic moment of $Fe^{2+}$ is about 4/5 the one of $Fe^{3+}$, a change in the ratio from 8.5 to 2 [as quantified in Fig. 3(a) for samples doped with 1 and 24 at.%, respectively] would

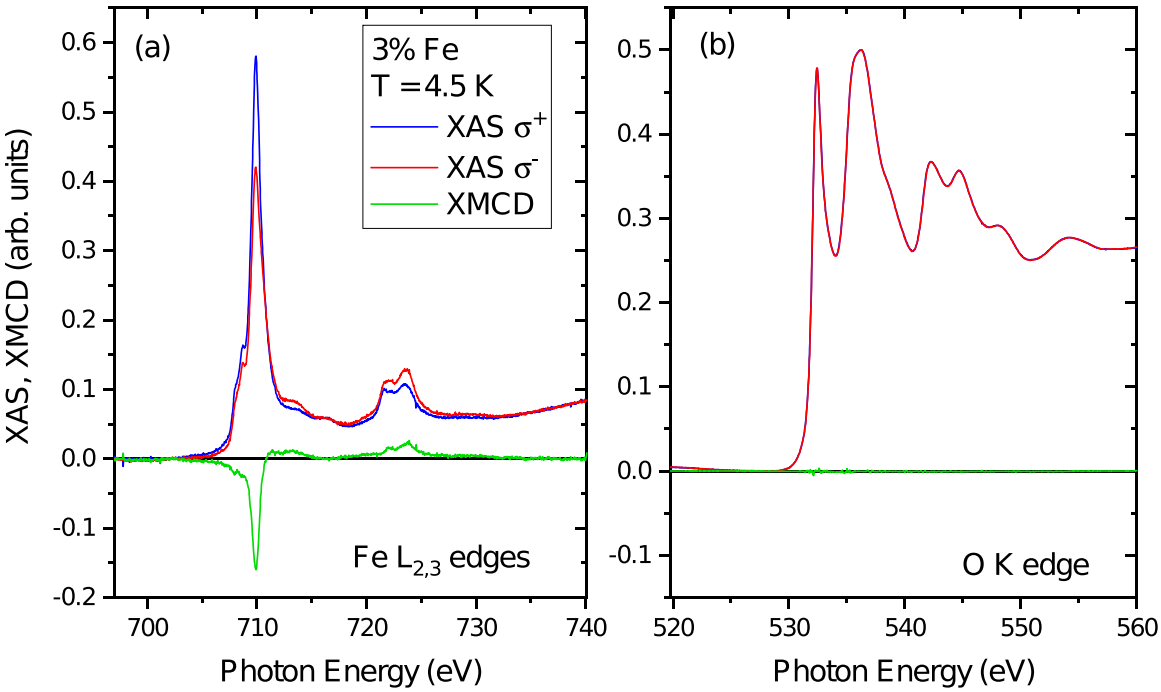


FIG. 2. Absorption spectra taken with opposite photon helicity (red and blue), and corresponding XMCD spectra (green), measured at (a) the Fe $L$ edges and (b) O $K$ edge. These measurements are referred to the sample with 3% Fe concentration, at 4.5 K with an applied field of 6 T. The lineshape is representative for all the samples. The spectra were rescaled so that the isotropic XAS spectra (the sum of left- and right-circularly polarized spectra, not shown in the figure) is normalized between 0 and 1.

produce a variation of the total magnetic moment by less than 10%. Instead, the most diluted sample has a signal more than three times bigger than the one with the highest doping level. This suggests that a significant change in the magnetic interaction between the Fe atoms should happen with varying concentration. A mechanism to explain this aspect is proposed in the next section.

While the spectral features of the XANES spectra are completely unaffected by the increase in the measuring temperature, the XMCD signal strongly changes. Figure 4 shows the behavior of the XMCD signal at the Fe $L_3$ edge as a function of the measuring temperature for the different samples. The XMCD signal asymptotically decreases with temperature to reach almost zero for temperatures higher than 50 K. Comparing different samples, we observe a slightly different behavior in the low-temperature dependence of the XMCD signal. For concentrations up to 11%, the measured XMCD increases almost linearly between 10 and 4.5 K. Instead, in samples doped with 15 to 24 at.% this increase is less pronounced and resembles a saturation of the magnetic signal below 10 K. This is shown in the inset of Fig. 4. This may be a symptom of antiferromagnetic coupling between Fe atoms, in accordance with the simulations presented in the next section. Frustrated magnetic interactions due to disorder or competing FM/AFM coupling may also be at the origin of the observed behavior.

The results obtained by fitting XMCD versus T curves with a Langevin function are summarized in Fig. 3(c) and are in good agreement with those obtained by applying the sum rules analysis to the XANES/XMCD spectra [Fig. 3(d)]. $m_{\text{spin}}$ and $m_{\text{orb}}$ are parallel [Fig. 3(d)], the $m_{\text{orb}}/m_{\text{spin}}$ ratio is dominated by $m_{\text{orb}}$, while the total magnetic moment ($m_{\text{tot}} = m_{\text{spin}} + m_{\text{orb}}$) [Fig. 3(c)] is governed by $m_{\text{spin}}$. $m_{\text{orb}}$ is almost constant for all Fe dopant concentrations, while both $m_{\text{spin}}$ and $m_{\text{tot}}$ decrease showing a plateau for Fe concentration in the 6 to 15 at.% range.

It is interesting to notice that the highest magnetic moment measured is actually close in magnitude with that of metallic iron (which is 2.2 $\mu_B$). In paramagnetism, the magnetic behavior is determined by the ratio $\mu H/k_B T$ (the argument of the Langevin function in the classical model of paramagnetism). For a magnetic moment of 1 or 2 Bohr magnetons, with a field of 6 T and at 5 K, the ratio would be still below 2. In these conditions, thermal agitation is still significant and the average magnetization should be less than half of its saturated value. Moreover, the magnetization should be linearly dependent from the applied field. The high magnetic response measured suggests that the system shows a high susceptibility and/or a high magnetic moment, not expected for a typical paramagnet. Further, if we compare the data measured at 6 and 1 T in Fig. 3(b) we see that the two data sets do not differ by just a multiplicative factor [see Fig. 3(b), data at $H = 6$ T rescaled]. This is a hint of the fact that at low doping concentration, the system may be in a regime in which the $M(H)$ relationship is not linear, i.e., the system is somehow closer to the saturation regime. This is something usually observed in super-PM systems due to the fact that the "elementary" magnetic moments that behave paramagnetically are very big since they originate from a large ensemble of interacting atoms. Hence in super-PM systems the susceptibility is usually big and the system can be saturated at reasonable fields.

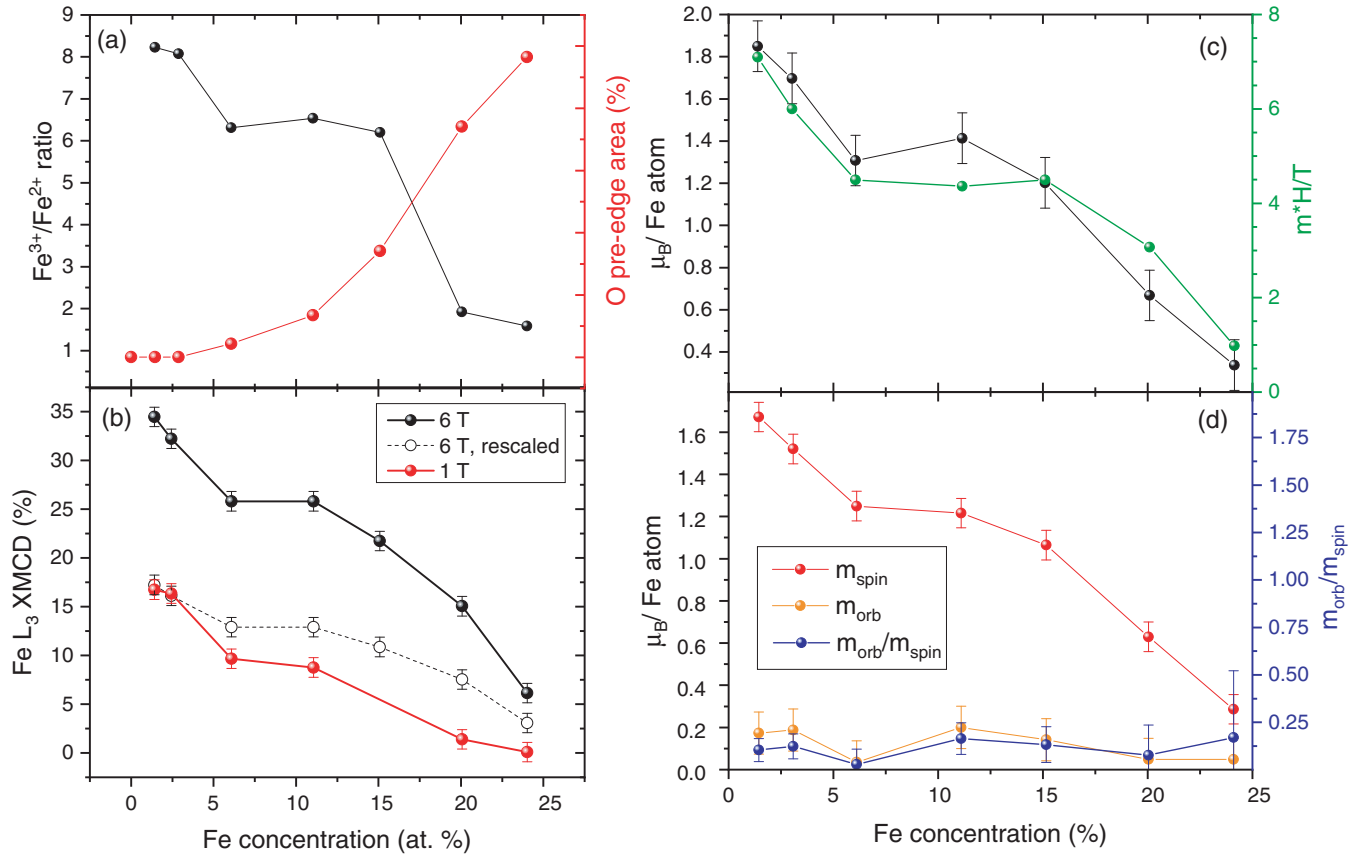


FIG. 3. (a) The $Fe^{3+}/Fe^{2+}$ ratio and the O pre-edge peak area (from Ref. [43]) and (b) the Fe $L_3$ XMCD signal as a function the dopant concentration. $T = 5$ K. (c) Comparison of the trend of $m_{tot}$ obtained by applying the sum rule analysis to the XANES spectra and $(\mu H)/T$ obtained by fitting the Fe $L_3$ XMCD signal as a function of the temperature with a Langevin function and (d) $m_{orb}$, $m_{spin}$, and $m_{orb}/m_{spin}$ ratio as a function of the dopant concentration.

### III. COMPUTATIONAL RESULTS

To identify the microscopic mechanisms responsible for magnetic coupling in Fe-doped $ZrO_2$, we performed first-principles simulations by plane-wave pseudopotential techniques of $Zr_{1-x}Fe_xO_{2-y}$, with $x = 6.25$ at.%, a concentration where both FM coupling (at diluted doping) and mechanisms responsible for its degradation (at moderate/high doping) are expected according to the experimental data. We used a 95 atoms super-cell of $ZrO_2$ containing two Fe and one O vacancy ($V_O$), which is located in the nearest-neighbor (NN) O-shell of one substitutional Fe to Zr, denoted as $Fe_1$, while the position of the other Fe atom, $Fe_2$, varies over all substitutional Zr sites of the supercell. After atomic relaxation, the $V_O$ migrates in the next NN O-shell to $Fe_1$, so $Fe_1$ in the relaxed structure has a NN shell composed of four O and has a $V_O$ in the next NN O-shell that is composed of three O. At variance, the $Fe_2$ is at the center of two neighbor (NN and next NN) O-shells composed of four O each, which is also the shell structure of O surrounding the Zr in fluorite zirconia. In the simulations, the number of O atoms in a given shell can be unambiguously determined, and by comparison with the bulk case (without vacancies) the number of O vacancy in one shell can be easily computed. At variance, the assignment of an exact position to the O vacancy in that shell can be questionable (since, in general, none of the O present in the shell with a O vacancy has conserved its original bulk position). For this reason, we do not indicate a position of an O vacancy in left panels of Figs. 6 and 8, where we display the relaxed atomic structure

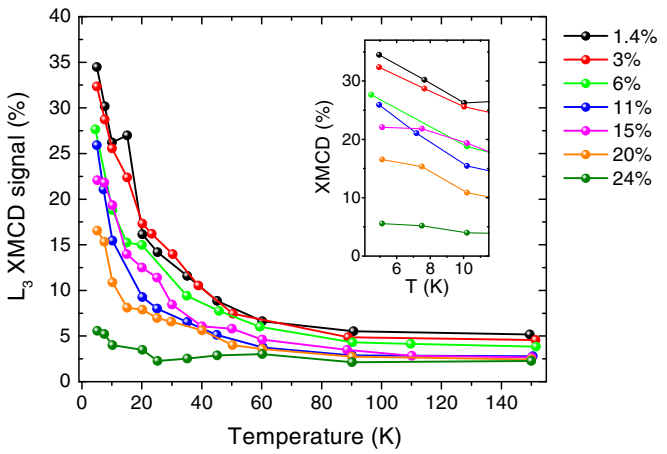


FIG. 4. Fe $L_3$ XMCD signal, for the investigated Fe concentrations, as a function of the temperature. The external magnetic field is equal to 6 T.

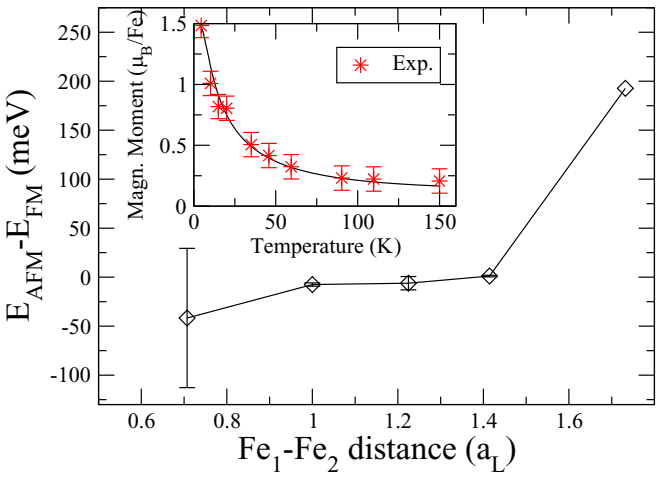


FIG. 5. First-principles simulation of $Zr_{1-x}Fe_xO_{2-x/2}$ with $x = 0.0625$. Shell average (mean and standard deviation) of the energy difference between fully relaxed AFM and FM spin configurations. The shell structure is defined according to Zr sublattice of bulk $ZrO_2$ fluorite that is also used to express the distance (in crystal units $a_L$) of a shell from the central atom. Insert: Magnetic moment (in Bohr magneton) per Fe atom as a function of temperature obtained by solving a mean field model (solid black line) and by applying the sum rule analysis to the XANES spectra (red stars)

for two different Fe-Fe configurations, but rather we limited the discussion of the position and the role of O vacancies in the text.

For each atomic configuration ($Fe_1$, $Fe_2$) we computed the total energy of both the FM ($E^{TOT}_{FM}$) and AFM ($E^{TOT}_{AFM}$) relaxed structures. The difference, that to a first approximation can be considered proportional to the exchange coupling parameter $J \propto \Delta E_J \equiv E^{TOT}_{AFM} - E^{TOT}_{FM}$, is a function of the Fe-Fe distance and of the angle formed by $Fe_2$ with the $Fe_1$-$V_O$ complex. In the following discussion, we will ignore the O sublattice and consider only the Zr sublattice in which the Fe are substitutional to Zr sites arranged according to the pristine fluorite structure, which is taken as a reference to determine the partition into shell and also the distance (reported in Fig. 5) from an atom ($Fe_2$) in a given shell to the central atom ($Fe_1$) [33]. In the chosen supercell, $Fe_1$ is surrounded by 5 Zr-shells at increasing distance from the central $Fe_1$. $Fe_2$ is placed in one substitutional site of the *nth* shell (with $n = 1, 2, 3, 4, 5$). For each shell we averaged $E^{TOT}_{AFM} - E^{TOT}_{FM}$ over all the $Fe_2$ configurations; in Fig. 5, we display our results for the mean and the standard deviation as a function of the $Fe_1$-$Fe_2$ distance.

When $Fe_2$ is placed in the first NN Zr-shell to $Fe_1$, the magnitude and the sign of the exchange interaction varies significantly among all distinct 12 configurations, from FM to AFM coupling, due to the presence of $V_O$ close to both Fe atoms, thus producing a large standard deviation. The atomic configuration of the ground state, in which $Fe_1$ and $Fe_2$ are NNs in Zr-lattice is displayed in Fig. 6 and presents a significant AFM coupling of the two Fe with $\Delta E_J = -105$ meV.

Among all possible $Fe_1$-$Fe_2$ configurations allowed by the supercell size, the more energetically favored FM state has an energy 0.15 eV higher than that of the ground state, corresponding to the configuration we denoted as FAR, in which $Fe_2$ is placed in the farthest shell of the supercell, i.e., the distance between each Fe and its nearest Fe is the maximum allowed by an uniform dopant distribution with $x = 6.25$ at.%.

For $Fe_2$ in the intermediate shells ($n = 2, 3, 4$), $\Delta E_J$, proportional to the exchange interaction, is very small, of the

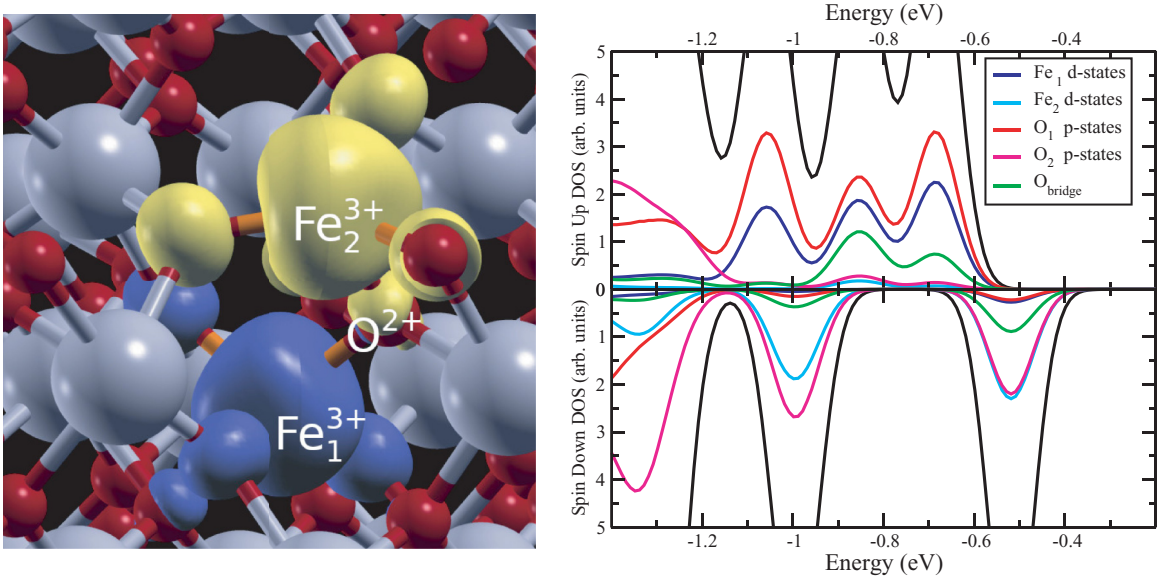


FIG. 6. Left panel: The atomic configuration of the antiferromagnetic ground state of $Zr_{1-x}Fe_xO_{2-x/2}$ with $x = 0.0625$. The symbol $O^{2+}$ labels the O in *bridge* position between two Fe. The isosurface (at 0.007 a.u.$^{-3}$ corresponding to ~1% of the maximum of the valence spin-density) for the spin-up (yellow) and spin-down (blue) density of states is also displayed. Right panel: The corresponding total (black solid line) and projected (colored solid line) density of states, normalized to the supercell. The zero of the energy scale corresponds to the Fermi energy.

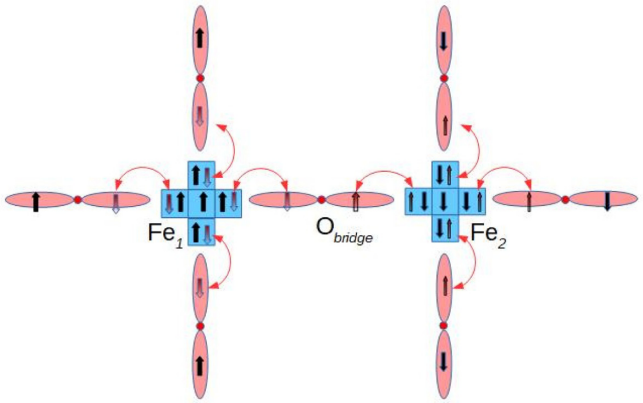


FIG. 7. The superexchange scheme of antiferromagnetic coupling. Light blue denotes Fe orbitals (squares: *d*-states). Light red denotes O orbitals (double ellipses: *p*-states). A red line connects the same spin-polarized electron (denoted by shadow red arrow) occupying a hybrid bond shared by two nearest-neighbor atoms.

order of a few meV, thus providing a PM contribution, and does not vary significantly within the same shell among the different $Fe_2$ configurations.

The magnetism is thus determined by two competing mechanisms: the AFM coupling when two substitutional Fe are NNs in the Zr-sublattice, and the FM coupling when two substitutional Fe are far apart.

### A. Antiferromagnetic ground state

At first, we analyze the AFM ground state, having $Fe_2$ positioned in the first Zr-shell to $Fe_1$. Since, according to our analysis, the main contribution to magnetization relies on Fe *d*-orbitals and O *p*-orbitals, in the following discussion and in the scheme of the magnetic interaction (Fig. 7) we refer to these orbitals only, while minor contributions from *s*-states are neglected.

The relaxed atomic configuration of the AFM ground state is displayed in Fig. 6. After atomic relaxation each Fe is surrounded by a shell of four O atoms, one of these oxygens, denoted as $O_{bridge}$, is shared by the two shell resulting in a "bridge" position between the two Fe. The angle $\theta$ formed by the $Fe_1$-$O_{bridge}$-$Fe_2$ bonds is $\theta = 112^\circ$, compatible with an AFM coupling that is proportional to $[\cos(\theta)]^2$ [34]. The AFM coupling is due to the superexchange interaction among the spin polarized *d*-states of Fe, mediated by the *p*-orbital of the $O_{bridge}$. The scheme for O-mediated superexchange interaction among two Fe is displayed in Fig. 7; the $Fe_1$-$O_{bridge}$-$Fe_2$ structure reproduces the standard scheme coupling two $Fe^{3+}$ [34,35]. It is worth noticing that, as a result of the difference in the oxidation state of the Zr and its substitutional Fe, the four O surrounding the Fe are partially polarized, as can be noticed in Fig. 6 (left panel) looking to the isosurface of the spin polarized valence electron density. The $O_{bridge}$ participates to the exchange interaction, and its magnetic moment (obtained by projecting the spin-resolved electron valence density on atomic orbitals) basically vanishes ($\sim 0.08\,\mu_B$), while the other three O of each NN shell present a small spin polarization ($\sim 0.2\,\mu_B$) due to hybridization of the O (mainly *p*) and Fe (mainly *d*) valence states. The spin polarization of these O is the same of the Fe they surround and is due to a partial charge transfer from O *p*-orbitals to Fe *d*-orbitals. The charge transfer involves the nearest neighbor O to each Fe resulting in global transfer of one electron to the Fe *d*-orbital and the consequent partial polarization of the *p*-states of the surrounding O, according to Hund's rule applied to the hybrid *pd*-orbitals. The scheme is illustrated by the six O (three O for each Fe) not in the *bridge* position in Fig. 7. Since this charge transfer mechanism (due to hybridization) does not change the overall magnetization of the Fe and its nearest-neighbor O, the Fe can still be considered in the $Fe^{3+}$ oxidation state with the advice that the corresponding five spin-polarized electrons now occupy five hybrid *pd* orbitals (O-*p* and Fe-*d* states) instead of the usual five Fe *d*-orbitals.

This superexchange interaction is clearly shown in the projected density of states (DOS) displayed in Fig. 6 (right panel) where is reported the energy range corresponding to the upper part of the valence bands (a more complete plot of the projected DOS is reported in Appendix C 2). The structure at energy lower that $-1.2$ eV originates from the electronic valence states of zirconia, while the peak structure at higher energy (from $-1.2$ eV up to $-0.4$ eV) represents the occupied electronic states in the bandgap of (undoped) zirconia and are due to the interaction of each Fe with its four nearest neighbor O, producing the above-mentioned orbital hybridization. By looking to the spin up DOS of Fig. 6 (right panel), in the energy range from $-1.2$ to $-0.6$ eV, the three peaks produced by the *p*-orbitals (red line) of the three O (denoted as $O_1$, with $O_1 \neq O_{bridge}$) surrounding $Fe_1$ are superimposed to the corresponding peaks produced by the *d* orbitals of $Fe_1$ (blue line), resulting in an hybridization of *pd*-orbitals at the same energy. In a similar way, by looking to the spin down DOS of Fig. 6 (right panel), in the energy range from $-1.1$ to $-0.4$ eV, the two peaks produced by the *p*-orbitals (magenta line) of the three O (denoted as $O_2$, with $O_2 \neq O_{bridge}$) surrounding $Fe_2$ are superimposed to the corresponding peaks produced by the *d* orbitals of $Fe_2$, resulting in a hybridization of *pd*-orbitals at the same energy, as well. In the energy range under consideration, the *p*-orbital DOS of $O_{bridge}$ (green line) presents the following. (i) Two peaks in the spin-up DOS that are superimposed to the two peaks (at about $-0.85$ and $-0.68$ eV) corresponding to the *pd*-orbitals of $O_1$ and $Fe_1$. (ii) Two peaks in the spin-down DOS that are superimposed to the two peaks (at about $-1.00$ and $-0.52$ eV) corresponding to the *pd*-orbitals of $O_2$ and $Fe_2$. The asymmetry in the spin-up and spin-down DOS as well as the presence of a very small magnetization of the $O_{bridge}$ can be attributed, at least in part, to the asymmetry in the coupling due to the presence of a O vacancy. The presence of both spin-up and spin-down peaks in the *p*-DOS of $O_{bridge}$ couples AFM the two Fe (and other nearest neighbor O of each Fe, trough hybrid orbitals), enlightening the microscopic mechanism responsible of AFM coupling produced by the superexchange interaction.

### B. Ferromagnetic state for Fe uniform distribution

Now we analyze the FM coupling of the FAR configuration, where the two Fe are placed at the maximum relative

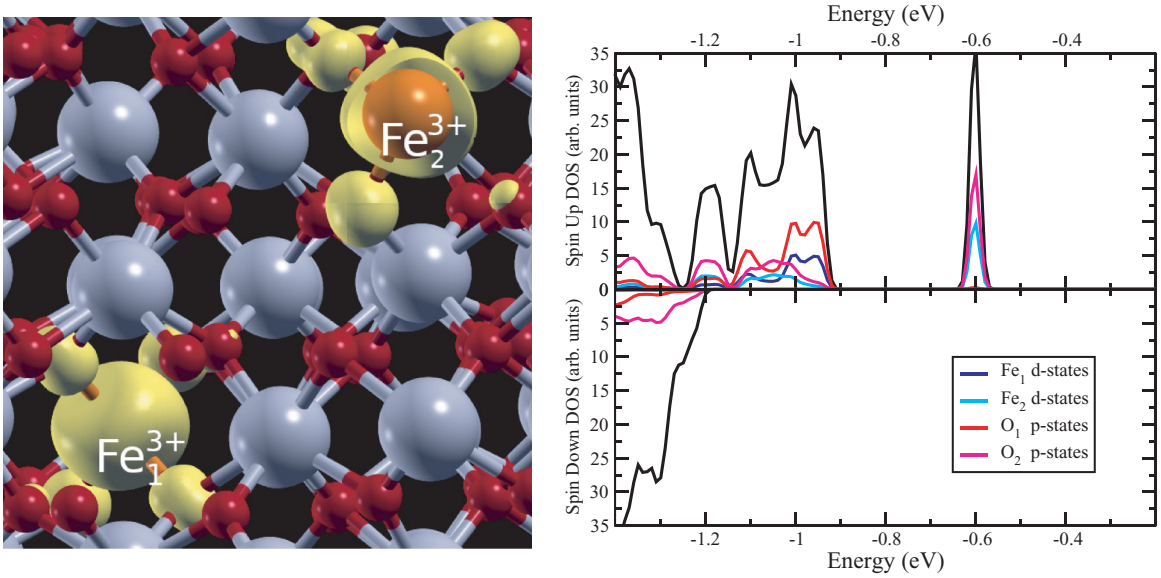


FIG. 8. Left panel: The atomic configuration of the ferromagnetic state with lower energy of $Zr_{1-x}Fe_xO_{2-x/2}$ with $x = 0.0625$. The isosurface (at 0.007 a.u.$^{-3}$ corresponding to ∼1% of the maximum of the valence spin-density) for the spin-up (yellow) density of states is also displayed. Right panel: The corresponding total (black solid line) and projected (colored line) density of states, normalized to the supercell. The zero of the energy scale corresponds to the Fermi energy.

distance compatible with periodic boundary conditions, thus corresponding to the configuration in which the Fe are uniformly distributed in the supercell (or in the whole crystal).

The relaxed atomic configuration of the FM ground states is displayed in Fig. 8 (left panel). After atomic relaxation, each Fe is surrounded by a NN shell of four O atoms that are partially polarized, as can be noticed by looking to the isosurface of the spin polarized valence electron density displayed in Fig. 8.

We propose that FM coupling of the two Fe can be explained by a superexchange-like mechanism [35] by considering the hybridization of Fe $d$ and $s$-orbitals with $sp$-orbitals of the four O NNs to the Fe.

This hybridization produces semicovalent oriented bonds that are filled according to the Hund's rule. Since some bonds participating to hybridization are empty, an electron with the same spin-orientation of Fe magnetic moment occupies the hybrid-orbitals formed by Fe and its 4-NNs O, resulting in a polarized bond oriented according to the local disposition of NN-O surrounding the Fe. The FM interaction is mediated by O through superexchange mechanisms. An illustrative scheme is displayed in Fig. 9, where the top left Fe ($Fe_1$) presents a semi-empty hybrid bond (of 4$s$ nature) partially occupied by a spin-up electron shared with the $sp$ orbital of NN O, according to the superexchange mechanism described above (see also Appendix C 2). This spin polarization of the O bonds can propagate through the crystal by means of the $sp$-orbitals of other O, the latter orbitals do not present a net magnetic moment, but rather a "spatial" polarization of orbitals of opposite spin (represented by the O with two black arrows in the middle of Fig. 9 and labeled as $O^{2-}$) caused by the partial hybridization with $sp$-orbital of O that are NN to the Fe. If one of the ("propagated") polarized O-bonds hybridizes with the $d$-orbitals of an other Fe ($Fe_2$), a FM coupling between the two Fe occurs.

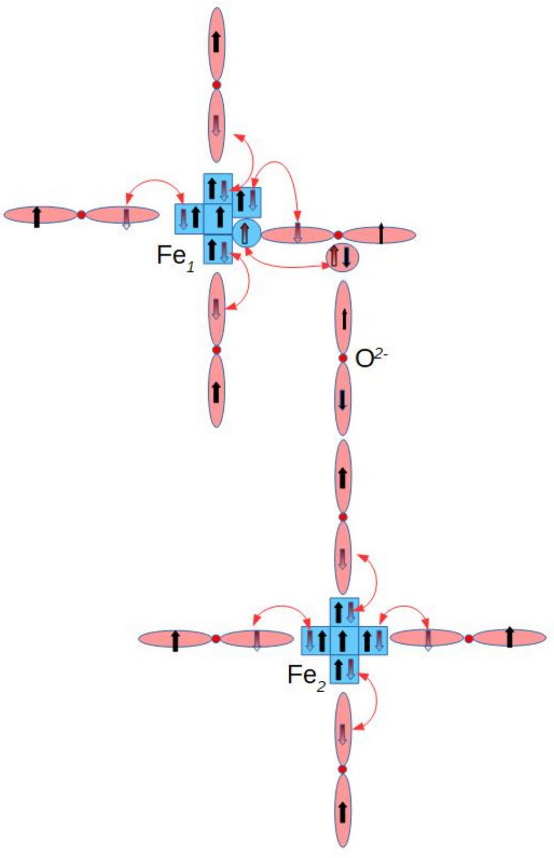


FIG. 9. The superexchange scheme of ferromagnetic coupling. Light blue denotes Fe orbitals (squares: $d$-states; circle: $s$-states). Light red denotes O orbitals (double ellipses: $p$-states; circle: $s$-states). A red line connects the same spin-polarized electron (denoted by shadow red arrow) occupying a hybrid bond shared by two nearest-neighbor atoms.

The FM coupling of $d$-states of each Fe with $p$-states of its NN-O is visible in the projected DOS in Fig. 8, where the contribution to the DOS originated from the orbitals forming hybrid semicovalent bonds are superimposed at the same energy, while for the role played by $s$-orbitals the reader can refer to Appendix C 2. In the right panel of Fig. 8, $O_1$ and $O_2$ denotes the sum of $p$-orbitals DOS of the four O in the NN shell to $Fe_1$ and $Fe_2$, respectively. In the energy range from $-1.2$ to $-0.9$ eV, the $Fe_1$ $d$-states (blue line) can hybridize with the $O_1$ $p$-states (red line) at the same energy, the same is true also for $Fe_2$ $d$-states (turquoise line) and $O_2$ $p$-states (magenta line). Further, the O in the next NN shell to $Fe_1$ and $Fe_2$ have a similar, but smaller, $p$-DOS structure in this energy range as the O in the NN shell. As a result, the polarization of O $p$-orbitals induces a FM coupling between the two Fe. As a fingerprint of the asymmetric coupling between $Fe_1$ and $Fe_2$ (Fig. 9) we notice that the polarization, originated also by the presence of $Fe_1$-$V_O$ complex, blue-shifts the semicovalent bonds formed by $Fe_2$ with its NN-O (turquoise and magenta peaks at $-0.6$ eV in Fig. 8) at an energy higher that the one of the corresponding peak of semicovalent bonds formed by $Fe_1$ with its NN-O (blue and red peaks at $-1.0$ eV in Fig. 8).

Incidentally, the presence of space-oriented hybrid bonds also explains the large standard deviation of $\Delta E_J$ in Fig. 5 for the first shell.

## IV. DISCUSSION

In light of the theoretical results, we propose that the measured magnetic behaviors can be explained, at least qualitatively, as follows. The chemical disorder, due to the random Fe distribution in Zr-sublattice, produces fluctuations of the Fe-Fe distance. So, for a random distribution of Fe in the Zr sub-lattice the PM, FM, and AFM interactions can coexist according to the different mutual Fe distances and arrangements. In general, if two (or few) Fe are FM coupled but their coupling with surrounding Fe is of PM nature, the system macroscopically behaves like a paramagnet [36]. A FM order, possible only assuming that a FAR configuration is extended on a macroscopic scale, has a statistically vanishing probability to be realized, due to random distribution of Fe. Furthermore, for a given concentration of randomly distributed Fe, the different magnetic couplings, due to the different Fe-Fe distances and arrangements, produce, also at low temperature, an average Fe magnetic moment (defined as the total magnetic moment divided by the number of Fe) that is only a fraction of the magnetic moment of a single Fe due to the presence of some AFM coupled Fe. Since the arrangements of Fe atoms creating a configuration similar to the FAR one are statistically possible only with configurations involving few Fe couples FM-ordered in limited-size regions of the sample, the formation of a long range magnetic order is prevented, but the system is paramagnetic and magnetically polarizable with a high magnetic moment per atom. Regions of the sample in which a FAR-like configuration is statistically generated by the random distribution of Fe can eventually develop FM ordering at the nanometer scale, typical of superparamagnetism. The similarity with super-PM systems should be investigated further with dedicated experiments. A hysteresis loop with finite coercivity should be detectable below the blocking temperature. Susceptibility measurements as a function of temperature should display significant differences in the Curie constant for samples which are simply PM and samples in which super-PM behaviors are present due to the difference in magnitude of the "effective" magnetic moments.

To verify that the mechanism proposed from first-principles simulations is compatible with the experimentally observed behavior, we can compare the Fe $L_3$ XMCD signal for $x = 6$ at.% at $H = 6$ T, shown in Fig. 4, with the corresponding theoretical magnetization as a function of temperature, displayed in the insert of Fig. 5, which has been computed, from our *ab initio* data for $x = 6.25$ at.%, by solving a mean field model with an external magnetic field of 6 T. As ingredients of the mean field model we used the exchange coupling coefficients estimated by the total energy approach, where the energy difference of the FM and AFM states are determined by our first-principles results. There are more sophisticated techniques to extract the exchange coupling coefficients, they are based on linear response [37] or frozen magnons [38]. However, such approaches — usually used to compute the critical Neél or the Curie temperature [39,40] — are beyond the scope of the present work aimed to determine the magnetic interaction at low temperature. To compute the trends of the magnetization as a function of temperature, the total energy approach adopted here is sufficient to bring out the principal features of the magnetic interaction in DMO as previously reported in the literature [39–41].

As can be noticed from the insert of Fig. 5 (see also Fig. 4), experimental and theoretical data show very similar behaviors. In spite of the simple model used (details in Appendix C 3), the computed average magnetization of $1.45\,\mu_B$ per Fe atom at a temperature of 5 K and an external magnetic field of 6 T, is in more than satisfactory agreement with the experimental value of $1.3\,\mu_B$ [displayed in Fig. 3(d)].

The AFM superexchange mechanism is responsible for the decrease in the magnetic signal as the Fe concentration increases, as shown in Fig. 3(b) [see also Figs. 3(c) and 3(d)]. In fact, for a uniform dopant distribution, the increase of Fe concentration produces a decrease of the average distance between two neighboring Fe. In particular, when the concentration is so large as to produce a significant probability to have two Fe in NN position in the Zr-sublattice, we expect a significant reduction in the magnetic signal. Assuming a uniform random distribution of Fe substitutional to Zr-sublattice, the critical site percolation concentration is $x_c \simeq 0.2$ [42], i.e., for this and for higher Fe concentration, the crystal is in an AFM state. In fact, if we imagine a "link" connecting two AFM-coupled Fe placed in NN sites of Zr-sublattice, then for $x > x_c$ the whole crystal can be imagined connected by a (figurative) "chain" composed of such links, producing an AFM. Significantly, for the sample with 24 at.%—thus having a concentration above the percolation threshold—the experimental magnetization practically vanishes suggesting the possibility of a transition to a fully AFM phase.

## V. CONCLUSION

By combining synchrotron data and *ab initio* simulations, we identified the bond-oriented superexchange mechanism as the responsible for the peculiar magnetic properties at low temperature in Fe-doped $ZrO_2$, producing paramagnetic interaction at diluted concentration. On the contrary, as the Fe concentration increases, the magnetic signal decreases, due to the O-mediated super-exchange AFM interaction, which prevails for a high Fe concentration in the range from 18 to 25 at.% i.e., a concentration at which a significant amount of Fe impurities, substitutional to Zr, are expected to interact through the superexchange mechanism mediated by an O located in a bridge position (Fe-O-Fe) between two neighboring Fe atoms.

## ACKNOWLEDGMENTS

Synchrotron radiation data were obtained at Helmholtz-Zentrum Berlin für Materialien und Energie (BESSY II) under Project No. 16204394. Samples were obtained within the framework of project OSEA (No. 2009-2552), financed by the CARIPLO foundation. Helpful discussions with J.M.D. Coey during the Joint European Magnetic Symposia (JEMS) 2019 are gratefully acknowledged. We acknowledge CINECA for computer resources allocated under ISCRA initiative (AIXAS), and R. Colnaghi for technical support on computer hardware.

## APPENDIX A: SAMPLE CHARACTERIZATION

Our samples, grown by atomic layer deposition [43], are composed of thin films of crystalline Fe-doped zirconia and show the crystal structure of fluorite. In the cubic (tetragonal) fluorite structure, the Zr cations are located in a face center cubic (tetragonal) lattice, and are surrounded by one (two) shell(s) of 8 (4) O located at the vertex of a cube (regular tetrahedron). At ambient condition, bulk zirconia usually presents the baddeleyite structure, a monoclinic phase, but the fluorite phase can be stabilized by doping [44] or by nanostructuring or by both [45]. However, in the doping stabilized fluorite phase, the two shells of four O surrounding the dopant in the tetragonal fluorite phase remain substantially distinguished also for high doping concentration in which the lattice parameters correspond to the cubic phase, a result well-established for isovalent doping by first principles in hafnia [46], and by combining *ab initio* calculation and synchrotron data in zirconia [47]. In thin films, as in the present case, due to surface effects, the grain size or the film geometry contribute to stabilize the doped fluorite structure [45].

In our samples, the film thickness, determined by elissometry, is about 19 nm [20,22]. Fe is uniformly distributed in the samples also at the higher concentration, as proved by transmission electron microscopy micro-analysis [21] and time-of-flight secondary ion mass spectrometry depth profiling [22,43]; the formation of Fe clusters can be excluded, within TEM resolution [21].

In zirconia, Fe is a substitutional impurity to $Zr^{4+}$, and is commonly present in the $Fe^{3+}$ oxidation state [20,48]. At diluted concentration, only a small fraction of Fe impurities present the $Fe^{2+}$ oxidation state. For charge neutrality, the Fe doping induces the formation of O vacancies ($V_O$), thus forming the compound $Zr_{1-x}Fe_xO_{2-y}$, with $y$ very close to $x/2$ [20], which corresponds to one $V_O$ every two Fe. Due to quenching, the magnetic moment of Fe ion is essentially the one associated to total spin: for $Fe^{3+}$ is $5/2$, while for $Fe^{2+}$ is 2.

## APPENDIX B: EXPERIMENTAL TECHNIQUES

X-ray absorption near edge spectroscopy (XANES) and x-ray magnetic circular dichroism (XMCD) at Fe $L_{2,3}$ and O $K$ edges have been collected at different temperatures ranging from 5 up to 150 K at UE49-PGM1 Beamline of BESSY synchrotron radiation source at Helmholtz-Zentrum Berlin (Germany). The spectra have been acquired in total electron yield (TEY) mode and normalized to the incident photon flux $I_0$, measured on a grid placed at the experimental chamber. All spectra were normalized by subtracting the signal background at the pre-edge and setting to one the intensity of the most intense peak.

The XMCD was measured applying an out-of-plane magnetic field of 6 T, the corresponding magnetic signals were evaluated as the difference between the spectra acquired with opposite photon helicities and taking into account the 75% circular polarization degree of light. The spin and orbital magnetic moment, $m_{\text{spin}}$ and $m_{\text{orb}}$ respectively, as a function of the measuring temperature and Fe dopant concentration, were calculated by applying the sum rule analysis [49,50] after subtraction of a two-step-function background from the raw XANES spectra. For the electron hole number of $3d$ orbital of Fe a value of 6.61 has been used [50,51]. The total magnetic moment $m_{\text{tot}} = m_{\text{spin}} + m_{\text{orb}}$ was also evaluated by fitting the Fe-$L_3$ XMCD signal as a function of temperature with a Langevin function:

$$\text{XMCD}(T) \sim \frac{M(T)}{M_S} = \coth(a) - \frac{1}{a}, \tag{B1}$$

where $a = (\mu H)/(kT)$, $H$ is the applied magnetic field, $T$ the temperature, $k$ the Boltzmann constant, and $\mu$ the magnetic moment. The XMCD signal is directly proportional to $M(T)/M_S$ which is the ratio between the magnetization as a function of temperature and the saturation magnetization of the sample.

To check the establishing of an antiferromagnetic coupling among the Fe atoms, or the presence of a crystallographic texture, x-ray magnetic linear dichroism (XMLD) were performed acquiring the XANES spectra with vertical and horizontal linear polarization, changing the incidence angle of the x-ray beam from 0° to 70° (or normal and grazing incidence). Moreover, the samples have been subjected to a field cooling treatment with an applied field of 1T to quench the antiferromagnetic order, if present. The results ruled out an antiferromagnetic contribution to the magnetic properties of the system at any Fe dopant concentration.

Measurements performed on zirconia samples doped with Al, an element having the same oxidation states of Fe, ruled out the possibility of magnetic properties unrelated to the presence of Fe dopant.

## APPENDIX C: FIRSTPRINCIPLES SIMULATIONS

### 1. Computational techniques

We performed first-principles simulations of Fe doped zirconia in the framework of the density functional theory (DFT), by using plane-wave pseudopotential techniques to solve the Kohn-Sham equations and to compute structural and electronic properties, as implemented in the QUANTUM ESPRESSO (QE) package [52]. In our calculations we used ultrasoft pseudopotentials [53,54] in the separable form introduced by Kleinmann and Bylander [55], generated with a Perdew-Burke-Ernzerhof (PBE) exchange-correlation functional [56]. This generalized gradient approximation (GGA) is capable to reproduce XANES [25], XPS [20] experimental spectra, and oxidation states [20] of Fe-doped zirconia. The pseudopotential for Zr includes semicore states. We chose a 40 Ry cutoff radius for the electronic valence wave function, and 400 Ry cutoff radius for the charge density. We used smearing techniques with a broadening of 0.001 Ry. For comparison, all DOS (and projected DOS) are normalized to the supercell.

To simulate the magnetic properties of Fe doped zirconia we used a tetragonal supercell containing 95 atoms: 2 Fe, 30 Zr; 63 O; and one O vacancy. The Brillouin zone (BZ) is sampled with a $2 \times 2 \times 2$ Monkhorst-Pack grid [57] [to properly describe the Fermi surface in the antiferromagnetic (AFM) and in the ferromagnetic (FM) configuration] to have an error on the energy difference between the FM and AFM phase lower than 1 meV per formula unit. The error on the total energy is estimated to be lower than 0.4 meV per formula unit. The atomic positions and the lattice constant are fully relaxed by a Broyden relaxation [58] with a threshold on the forces of 0.25 meV/Å. The convergence thresholds are the same as the ones used in Ref. [43], where the interested reader can refer for further computation details.

To identify the microscopic mechanisms responsible for magnetic coupling in Fe-doped $ZrO_2$, we performed first-principles simulations of $Zr_{1-x}Fe_xO_{2-y}$ selecting the Fe concentration equal to 6.25 at.%. This choice of $x$ combines the needs for a computational affordable supercell size, with the one for a Fe concentration where both FM coupling (at diluted doping) and mechanisms responsible for the degradation of FM coupling (at moderate/high doping) are expected according to the experimental data displayed in the main text. The chemical disorder—i.e., Fe impurities substitutional to Zr, in which the dopants are randomly distributed in the Zr sublattice—and the geometric structure of the material are simulated by means of the supercell method with periodic boundary conditions. Fe atoms were placed at substitutional Zr sites. We considered a supercell with 32 $ZrO_2$ formula units in the undoped case, and simulating the doping with one O vacancy ($V_O$) per two substitutional Fe. The $V_O$ is assumed (for the unrelaxed structure) in the nearest-neighbor (NN) O-shell of one substitutional Fe to Zr, denoted as $Fe_1$, while the position of the other Fe atom, $Fe_2$, varies over all substitutional Zr sites of the supercell. After atomic relaxation, the NN and the next NN atomic shells to $Fe_2$ are composed of four O, following the arrangement of tetragonal fluorite, while the NN atomic shell to $Fe_1$ is composed of four O and the next NN atomic shell is composed of three O since, during the relaxation, the $V_O$ moves from the NN to the next NN O-shell to $Fe_1$.

In the discussion presented in the main text, we found convenient to display the *ab initio* results by performing the shell average of the quantity $\Delta E_J \equiv E^{\mathrm{TOT}}_{\mathrm{AFM}} - E^{\mathrm{TOT}}_{\mathrm{FM}}$, as described below. We place $Fe_1$ as substitutional impurity in a Zr site of the supercell and we consider the Zr shells surrounding $Fe_1$; for each shell we compute $\Delta E_J$ in all distinct configurations obtained by placing $Fe_2$ in one Zr site of the shell, and perform the average of $\Delta E_J$ over all different configurations having $Fe_2$ in the same shell. For simplicity, the average is computed (and reported) considering the Zr site of the shell corresponding to the cubic fluorite structure. In our simulations the $Fe_2$ is positioned in the shell of tetragonal fluorite corresponding to the sites in shell of cubic fluorite (i.e., neglecting the small distortion of FCC lattice in tetragonal fluorite), in which $c/a = 1$. Since, in the simulated tetragonal structure the c/a ratio is about 1.03 (while in cubic fluorite $c/a = 1$ by definition), in the distorted fluorite structure $Fe_2$ experiences a slightly different distance from central $Fe_1$, according to their position in shell. For clarity, we find convenient neglect this small difference in $Fe_1$-$Fe_2$ distances, in our discussion.

### 2. Superexchange mechanisms for FM coupling

Since the analysis of the ferromagnetic FAR configuration in terms of the superexchange mechanism requires drawing a more elaborate picture than the one used in the analysis of the antiferromagnetic ground state, we will provide a detailed description of a superexchange-like mechanism responsible of ferromagnetic interaction at diluted Fe concentrations. We explain the FM coupling obtained in the simulation of the FAR configuration, by considering the hybridization of Fe $d$- and $s$-orbitals with $sp$-orbitals of the four O NNs to the Fe. Bulk zirconia presents ionic bonds, but the presence of magnetic impurities causes partial hybridization of the orbital of Fe with the orbitals of the four O surrounding the Fe, thus producing semicovalent bonds. Since the semi-empty Fe $s$-orbitals strongly overlap the semifull $sp$-orbitals of NN O, the electrons occupying an O $sp$-orbital may spend some of their time in the Fe orbital. Because Fe has an oriented magnetic moment, these electrons will not have the same probability of being shared by the Fe. Due to the presence of the exchange interaction, the O electron whose spin is parallel to the Fe magnetic moment spends more time on the Fe than the one with the antiparallel spin. This behavior follows Hund's rule if one assumes that the shell of $d$ orbitals is extended by the $s$ and $p$ orbitals when hybrid orbitals are formed. As a result, an electron with the same spin-orientation of Fe magnetic moment occupies the hybrid-orbitals formed by Fe and its 4-NN O, resulting in a polarized bond oriented according to the local disposition of NN-O surrounding the Fe.

In Fig. 10 we display our results for the projected DOS on the $s$-orbitals for the two Fe and the corresponding NN O-shells. We notice the presence of three peaks of $Fe_1$ $s$-states in the energy range ($-1.25$ to $-0.90$ eV), i.e., at the same energy where the peaks of the $Fe_1$-$d$ and $O_1$-$p$ states are present, thus suggesting orbital hybridization also involving $s$ states. The presence of an almost empty $Fe_1$-$s$ orbital can support a FM

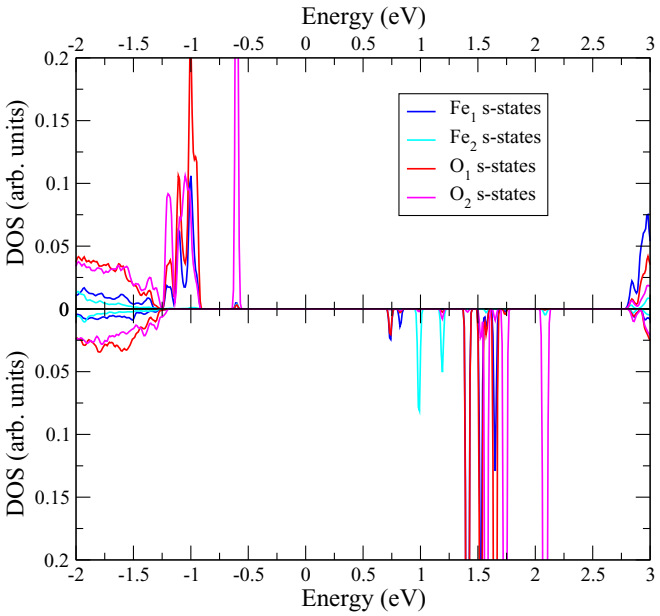


FIG. 10. The projected (colored solid lines) density of states, normalized to the supercell, corresponding to the ferromagnetic state with lower energy of $Zr_{1-x}Fe_xO_{2-x/2}$ with $x = 0.0625$. The zero of the energy scale corresponds to the Fermi energy.

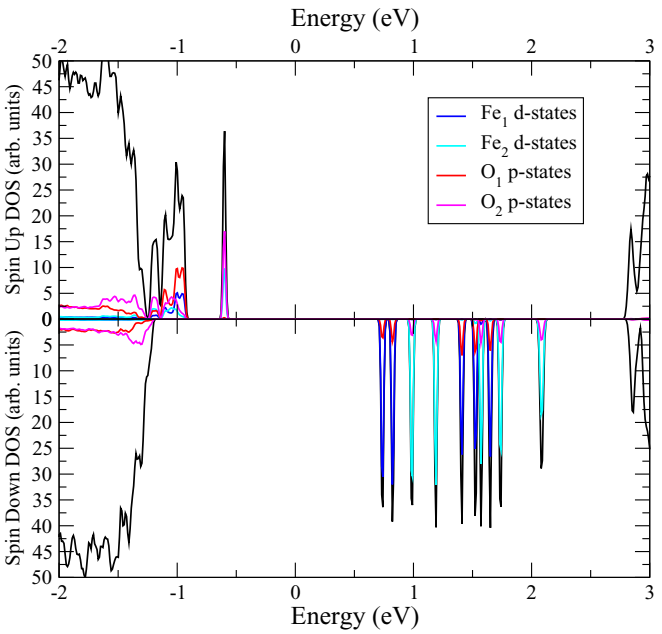


FIG. 11. The total (black solid line) and projected (colored solid lines) density of states, normalized to the supercell, corresponding to the ferromagnetic state with lower energy of $Zr_{1-x}Fe_xO_{2-x/2}$ with $x = 0.0625$. The zero of the energy scale corresponds to the Fermi energy.

coupling by O-mediated superexchange interaction, according to the scheme displayed in Fig. 9 of the main text. This scheme is supported by the presence in the same range, (−1.25 to −0.90 eV), also of peaks of $O_1$ and $O_2$ *s*-DOS (see Fig. 10) and of $O_1$ and $O_2$ *p*-DOS as well (see Fig. 8 main text), suggesting a O-mediated coupling between the $Fe_1$ *s*-states (Fig. 10), and the $Fe_2$ *d*-states, which present peaks in the same energy range (Fig. 8 main text).

The peaks at −0.6 eV denote the hybridization of *s*-orbitals of $O_2$ (Fig. 10) with $O_2$-*p* and $Fe_2$-*d* orbitals (Fig. 8 main text). Note the absence of any peak structure for the *s*-orbital of $Fe_2$ in the energy range (to 0.0 eV) both in spin up and spin down DOS since this state does not participate to the hybridization and this asymmetry in the hybridization process for $Fe_1$ and $Fe_2$ (that we attributed to the presence of the $V_O$) and the O-mediated interaction are responsible of the FM coupling of the two Fe.

For reference, in Figs. 11 and 12 we display the projected DOS of FM and AFM configurations displayed in the right panel of Figs. 8 and 6 of the main text, respectively, over a wider energy range.

### 3. Mean field model

To check the compatibility of our theoretical picture with the temperature behavior of XMCD signal, we computed the magnetization as a function of temperature, using our *ab initio* data, by solving a mean field two lattice model. The ingredients of this model are the exchange coupling parameters simulated *ab initio* for $Zr_{1-x}Fe_xO_{2-x/2}$ with $x = 0.0625$ [59]. For each configuration of $Fe_1$ and $Fe_2$ considered in the supercell, the exchange coupling constant is obtained from the *ab initio* data $\Delta E_J$ that has been used to reproduce the energy difference between the FM and the AFM configuration of the model Hamiltonian at absolute zero. In our study, we used the mean field two sub-lattice model, described, e.g., in Ref. [60] in which the exchange is restricted to magnetic ions in the nearest neighbor magnetic sublattice. In the present calculation, one magnetic sublattice corresponds to the periodically

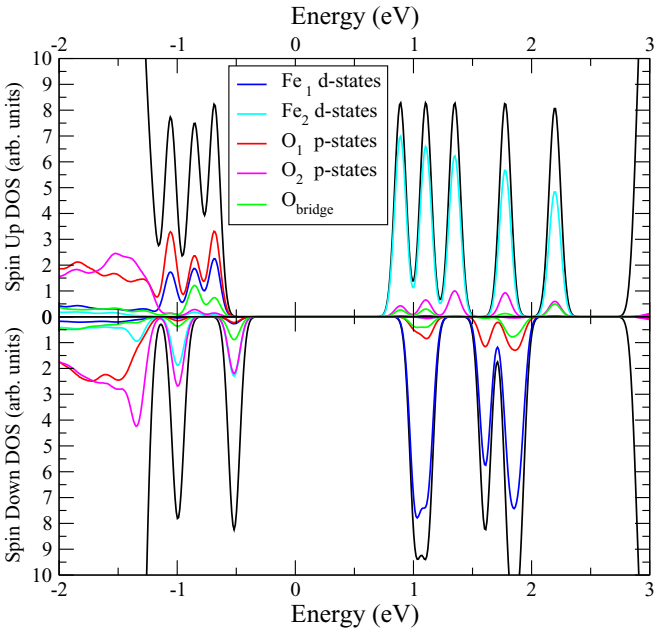


FIG. 12. The total (black solid line) and projected (colored solid lines) density of states, normalized to the supercell, corresponding to the antiferromagnetic ground state of $Zr_{1-x}Fe_xO_{2-x/2}$ with $x = 0.0625$. The zero of the energy scale corresponds to the Fermi energy.

repeated images of $Fe_1$ the other to the periodically repeated images of $Fe_2$. Due to quenching, the magnetic moment of Fe ion is the one associated to total spin $S$, which in our mean field model calculation is $S = 5/2$ corresponding to $Fe^{3+}$ oxidation state in agreement with our *ab initio* results and experimental finding. In the two-sublattice mean field Hamiltonian, each magnetic moment of an ion in $i$-sublattice is supposed to interact with an effective magnetic field $B^{\text{eff}}$ that includes the external magnetic field and the effect of the average interaction with other magnetic ions, that should be determined self consistently. The total Hamiltonian is: $H = H_1 + H_2$ where $H_i = -2\mu_0\mu_B \overrightarrow{S_i} \cdot \overrightarrow{B_i^{\text{eff}}}$ $(i = 1, 2)$. The reader interested in further details about the two-sublattice mean field model and to a discussion of the physical approximations involved and on the limit and capabilities of this method can refer to Ref. [60] and references therein. Notice that, due to periodic boundary conditions, the FAR configuration corresponds to a supercell having $Fe_2$ in the center surrounded by eight $Fe_1$ in the vertexes of the supercell ($Fe_1$ experiences the same configuration for translational symmetry), this cooperative effect generates the large observed FM coupling; however, for the FAR case, the exchange coupling of each $Fe_1$-$Fe_2$ couple is thus proportional to $\Delta E_J/8 = 24$ meV by assuming the interactions are additive and limited to nearest-neighbor Fe.

We computed the magnetization as a function of temperature, for each $Fe_1$-$Fe_2$ configuration considered. The $Fe_1$-$V_O$ complex is fixed in central position with respect to the 5 Zr-shells in which $Fe_2$ is placed according to the configuration considered. In our model, we assume that $Fe_2$ can occupy with equal probability each Zr site in the supercell. However, for each configuration of $Fe_2$ in a given shell, we assign a thermal weight (Boltzmann distribution), to take into account the thermal re-arrangement of O surrounding $Fe_1$ due to the presence of the O vacancy that can be caused by mobility of O vacancy in zirconia [61].


[1] T. Dietl and H. Ohno, Dilute ferromagnetic semiconductors: Physics and spintronic structures, Rev. Mod. Phys. **86**, 187 (2014).

[2] S. J. Pearton, W. H. Heo, M. Ivill, D. P. Norton, and T. Steiner, Dilute magnetic semiconducting oxides, Semicond. Sci. Technol. **19**, R59 (2004).

[3] S. Ostanin, A. Ernst, L. M. Sandratskii, P. Bruno, M. Däne, I. D. Hughes, J. B. Staunton, W. Hergert, I. Mertig, and J. Kudrnovský, Mn-Stabilized Zirconia: From Imitation Diamonds to a New Potential High-$t_c$ Ferromagnetic Spintronics Material, Phys. Rev. Lett. **98**, 016101 (2007).

[4] I. Zhitomirsky, M. Niewczas, and A. Petric, Synthesis and magnetic properties of ni-zirconia composites, Mater. Manuf. Process. **18**, 719 (2003).

[5] J. Zippel, M. Lorenz, A. Setzer, G. Wagner, N. Sobolev, P. Esquinazi, and M. Grundmann, Defect-induced ferromagnetism in undoped and mn-doped zirconia thin films, Phys. Rev. B **82**, 125209 (2010).

[6] X. Zhao, M. Wang, T. Wei, J. Ren, B. Wang, Y. Han, and Z. Zhao, Possible origin of ferromagnetism in transition metal doped zirconia, J. Supercond. Nov. Magn **31**, 2559 (2018).

[7] P. Pramanik, S. Singh, D. C. Joshi, A. Mallick, K. Pisane, A. H. Romero, S. Thota, and M. S. Seehra, Cubic phase stability, optical and magnetic properties of cu-stabilized zirconia nanocrystals, J. Phys. D-Appl. Phys. **51**, 225304 (2018).

[8] N. H. Hong, N. Poirot, and J. Sakai, Evidence for magnetism due to oxygen vacancies in fe-doped $HfO_2$ thin films, Appl. Phys. Lett. **89**, 042503 (2006).

[9] K. K. Bharathi, S. Venkatesh, G. Prathiba, N. H. Kumar, and C. V. Ramana, Room temperature ferromagnetism in $HfO_2$ films, J. Appl. Phys. **109**, 07C318 (2011).

[10] J. E. Jaffe, R. A. Bachorz, and M. Gutowski, Low-temperature polymorphs of $ZrO_2$ and $HfO_2$: A density-functional theory study, Phys. Rev. B **72**, 144107 (2005).

[11] N. H. Hong, C.-K. Park, A. T. Raghavender, O. Ciftja, N. S. Bingham, M. H. Phan, and H. Srikanth, Room temperature ferromagnetism in monoclinic mn-doped $ZrO_2$ thin films, J. Appl. Phys. **111**, 07C302 (2012).

[12] N. H. Hong, M. B. Kanoun, S. Goumri-Said, J.-H. Song, E. Chikoidze, Y. Dumont, A. Ruyter, and M. Kurisu, The origin of magnetism in transition metal-doped $ZrO_2$ thin films: experiment and theory, J. Phys.-Condes. Matter **25**, 436003 (2013).

[13] S. Kumar and A. K. Ojha, Room temperature ferromagnetism in undoped and mn doped t-$ZrO_2$ nanostructures ariginated due to oxygen vacancy and effect of mn doping on its optical properties, Mater. Chem. Phys. **169**, 13 (2016).

[14] K. Kalam, H. Seemen, P. Ritslaid, M. Rähn, A. Tamm, K. Kukli, A. Kasikov, J. Link, R. Stern, S. Dueñas, H. Castán, and H. García, Atomic layer deposition and properties of $ZrO_2/FeO_2$ thin film, Beilstein J. Nanotechnol. **9**, 119 (2018).

[15] S. Kumar, S. Bhunia, J. Singh, and A. K. Ojha, Absence of room temperature ferromagnetism in fe stabilized $ZrO_2$ nanostructures and effect of fe doping on its structural, optical and luminescence properties, J. Alloy. Compd. **649**, 348 (2015).

[16] T. R. Sahoo, S. S. Manoharan, S. Kurian, and N. S. Gajbhiye, Mössbauer spectroscopic study of iron-doped zirconia synthesized by microwave route, Hyperfine Interact. **188**, 43 (2009).

[17] I. Kuryliszyn-Kudelska, A. Arciszewska, M. Małolepszy, M. Mazurkiewicz, L. Stobinski, A. Grabias, M. Kopcewicz, W. Paszkowicz, R. Minikaev, V. Domukhovski, N. Nedelko, and W. Dobrowolski, Influence of fe doping on magnetic properties of $ZrO_2$ nanocrystals, J. Alloy. Compd **632**, 609 (2015).

[18] A. de Souza, F. F. Ivashita, V. Biondo, A. Paesano, and D. H. Mosca, Structural and magnetic properties of iron doped $ZrO_2$, J. Alloy. Compd. **680**, 701 (2016).

[19] J. M. D. Coey, Dilute magnetic oxides, Curr. Opin. Solid State Mater. Sci. **10**, 83 (2006).

[20] D. Sangalli, A. Lamperti, E. Cianci, R. Ciprian, M. Perego, and A. Debernardi, The role of oxygen vacancies on the structure and the density of states of iron doped zirconia, Phys. Rev. B **87**, 085206 (2013).

[21] D. Sangalli, E. Cianci, A. Lamperti, R. Ciprian, F. Albertini, F. Casoli, P. Lupo, L. Nasi, M. Campanini, and A. Debernardi, Exploiting magnetic properties of fe doped in zirconia. from first-principles simulations to the experimental growth and characterization of thin films, Eur. Phys. J. B **86**, 211 (2013).

[22] A. Lamperti, E. Cianci, R. Ciprian, D. Sangalli, and A. Debernardi, Stabilization of tetragonal/cubic phase in fe doped zirconia grown by atomic layer deposition, Thin Solid Films **533**, 83 (2013).

[23] P. Satyarthi, S. Ghosh, P. Pandey, B.and Kumar, C. L. Chen, C. L. Dong, W. F. Pong, D. Kanjilal, K. Asokan, and P. Srivastava, Coexistence of intrinsic and extrinsic origins of room temperature ferromagnetism in as implanted and thermally annealed zno films probed by x-ray absorption spectroscopy, J. Appl. Phys. **113**, 183708 (2013).

[24] T. Higuchi, K. Kobayashi, S. Yamaguchi, A. Fukushima, S. Shin, and T. Tsukamoto, Band structure of $TiO_2$ -doped yttria-stabilized zirconia probed by soft-x-ray spectroscopy, Jpn. J. Appl. Phys. **42**, L941 (2003).

[25] D. H. Douma, R. Ciprian, A. Lamperti, P. Lupo, E. Cianci, D. Sangalli, F. Casoli, L. Nasi, F. Albertini, P. Torelli, and A. Debernardi, Experimental versus *ab initio* x-ray absorption of iron-doped zirconia: Trends in o $k$-edge spectra as a function of iron doping, Phys. Rev. B **90**, 205201 (2014).

[26] L. Soriano, M. Abbate, J. C. Fuggle, M. A. Jiménez, J. M. Sanz, C. Mythen, and H. A. Padmore, The $O_1$s x-ray absorption spectra of transition-metal oxides: The $Tio_2$-$ZrO_2$-$HfO_2$ and $V_2O_5$-$Nb_2O_5$-$Ta_2O_5$ series, Solid State Commun. **87**, 699 (1993).

[27] D.-Y. Cho, H.-S. Jung, J. H. Kim, and C. S. Hwang, Monoclinic-like local atomic structure in amorphous $ZrO_2$ thin film, Appl. Phys. Lett. **97**, 141905 (2010).

[28] A. Kikas, J. Aarik, V. Kisand, K. Kooser, T. Käämbre, H. Mändar, T. Uustare, R. Rammula, V. Sammelselg, and I. Martinson, Effect of phase composition on x-ray absorption spectra of $ZrO_2$ thin films, J. Electron Spectrosc. Relat. Phenom. **156-158**, 303 (2007).

[29] M. Abbate, F. M. F. de Groot, J. C. Fuggle, A. Fujimori, O. Strebel, F. Lopez, M. Domke, G. Kaindl, G. A. Sawatzky, M. Takano, Y. Takeda, H. Eisaki, and S. Uchida, Controlled-valence properties of $La_{1-x}Sr_xFeO_3$ and $La_{1-x}Sr_xMnO_3$ studied by soft-x-ray absorption spectroscopy, Phys. Rev. B **46**, 4511 (1992).

[30] R. Kumar, A. P. Singh, P. Thakur, K. H. Chae, W. K. Choi, B. Angadi, S. D. Kaushik, and S. Patnaik, Ferromagnetism and metal-semiconducting transition in fe-doped ZnO thin films, J. Phys. D **41**, 155002 (2008).

[31] P. Wu *et al.*, Ferromagnetism in fe-implanted a-plane ZnO films, Appl. Phys. Lett. **89**, 012508 (2006).

[32] F. M. F. De Groot, P. Glatzel, U. Bergmann, P. A. van Aken, R. A. Barrea, S. Klemme, M. Hävecker, A. Knop-Gericke, W. M. Heijboer, and B. M. Weckhuysen, 1$s$2$p$ resonant inelastic x-ray scattering of iron oxides, J. Phys. Chem. B **109**, 20751 (2005).

[33] Although the total energies are computed after atomic relaxation, for convenience, in the presentation the distances in Fig. 5 are referred to as the pristine flourite structure, i.e., before relaxation since after relaxation atoms in the same shell can presents (slightly) different distances from the central atoms due to the asymmetry introduced by the O vacancy and by the different magnetic coupling (AFM/FM) considered.

[34] See, e.g., J. M. D. Coey, *Magnetism and Magnetic Materials* (Cambridge University Press, Cambridge, England, 2009).

[35] For an illustration of superexchange mechanism see, e.g., N. Spaldin, *Magnetic Materials* (Cambridge University Press, Cambridge, England, 2003); The interested reader can refer also to the original works: H. A. Kramers, Physica **1**, 182 (1934); P. W. Anderson, Phys. Rev. **79**, 350 (1950); J. B. Goodenough, *ibid.* **100**, 564 (1955).

[36] Similar result is expected also if the two (or few) FM coupled Fe have an AFM interaction with one Fe.

[37] A. I. Liechtenstein, M. I. Katsnelson, V. P. Antropov, and V. A. Gubanov, Local spin density functional approach to the theory of exchange interactions in ferromagnetic metals and alloys, J. Magn. Magn. Mater. **67**, 65 (1987).

[38] L. M. Sandratskii and P. Bruno, Exchange interactions and Curie temperature in (Ga,Mn)As, Phys. Rev. B **66**, 134435 (2002).

[39] A. Ramasubramaniam and D. Naveh, Mn-doped monolayer $MoS_2$: An atomically thin dilute magnetic semiconductor, Phys. Rev. B **87**, 195201 (2013).

[40] Y. D. Park, A. T. Hanbicki, S. C. Erwin, C. S. Hellberg, J. M. Sullivan, J. E. Mattson, T. F. Ambrose, A. Wilson, G. Spanos, and B. T. Jonker, A group-IV ferromagnetic semiconductor: $Mn_xGe_{1-x}$, Science **295**, 651 (2002).

[41] P. Mahadevan, A. Zunger, and D. D. Sarma, Unusual Directional Dependence of Exchange Energies in GaAs Diluted with Mn: Is the RKKY Description Relevant? Phys. Rev. Lett. **93**, 177201 (2004).

[42] N. Ce-Wen, Percolation phenomena in the stabilized cubic zirconia solid solution, Mater. Sci. Eng. **B3**, L1 (1989).

[43] A. Lamperti, E. Cianci, R. Ciprian, L. Capasso, E. Weschke, and A. Debernardi, Magnetic properties of iron doped zirconia as a function of fe concentration: From *ab initio* simulations to the growth of thin films by atomic layer deposition and their characterization by synchrotron radiation, J. Vac. Sci. Technol. A **36**, 02D404 (2018).

[44] D. Sangalli and A. Debernardi, Exchange–correlation effects in the monoclinic to tetragonal phase stabilization of yttrium–doped $ZrO_2$: a first-principles approach, Phys. Rev. B **84**, 214113 (2011).

[45] A. Debernardi, D. Sangalli, A. Lamperti, E. Cianci, P. Lupo, F. Casoli, F. Albertini, L. Nasi, R. Ciprian, and P. Torelli, Electronic and magnetic properties of iron doped zirconia: Theory and experiment, J. Appl. Phys. **115**, 17D718 (2014).

[46] A. Debernardi, *Ab initio* study of phase transition and dielectric constants of high-$\kappa$ $HfO_2$ as a function of Ge alloying, Phys. Rev. B **85**, 024109 (2012).

[47] F. Boscherini, F. D'Acapito, S. F. Galata, D. Tsoutsou, and A. Dimoulas, Atomic scale mechanism for the ge-induced stabilization of the tetragonal, very high-$\kappa$, phase of $ZrO_2$, Appl. Phys. Lett. **99**, 121909 (2011).

[48] P. Madkikar, D. Menga, G. S. Harzer, T. Mittermeier, A. Siebel, F. E. Wagner, M. Merz, S. Schuppler, P. Nagel, A. B. Muñoz García, M. Pavone, H. A. Gasteiger, and M. Piana, Nanometric fe-substituted $ZrO_2$ on carbon black as pgm-free rr catalyst for pemfcs, J. Electrochem. Soc. **166**, F3032 (2019).

[49] T. Koide, H. Miyauchi, J. Okamoto, T. Shidara, T. Sekine, T. Saitoh, A. Fujimori, H. Fukutani, M. Takano, and Y. Takeda, Close correlation between the magnetic moments, lattice distortions, and hybridization in $LaMnO_3$ and $La_{1-x}Sr_xMnO_{3-\delta}$: Doping-Dependent Magnetic Circular X-Ray Dichroism Study, Phys. Rev. Lett. **87**, 246404 (2001).

[50] C. T. Chen, Y. U. Idzerda, H.-J. Lin, N. V. Smith, G. Meigs, E. Chaban, G. H. Ho, E. Pellegrin, and F. Sette, Experimental Confirmation of the X-Ray Magnetic Circular Dichroism Sum Rules for Iron and Cobalt, Phys. Rev. Lett. **75**, 152 (1995).

[51] A. Langenberg, K. Hirsch, A. Ławicki, V. Zamudio-Bayer, M. Niemeyer, P. Chmiela, B. Langbehn, A. Terasaki, B. V. Issendorff, and J. T. Lau, Spin and orbital magnetic moments of size-selected iron, cobalt, and nickel clusters, Phys. Rev. B **90**, 184420 (2014).

[52] P. Giannozzi, S. Baroni, N. Bonini, M. Calandra, R. Car, C. Cavazzoni, D. Ceresoli, G. L. Chiarotti, M. Cococcioni, I. Dabo, A. Dal Corso, S. Fabris, G. Fratesi, S. de Gironcoli, R. Gebauer, U. Gerstmann, C. Gougoussis, A. Kokalj, M. Lazzeri, L. Martin-Samos, N. Marzari, F. Mauri, R. Mazzarello, S. Paolini, A.r Pasquarello, L. Paulatto, C. Sbraccia, S. Scandolo, G. Sclauzero, A. P. Seitsonen, A. Smogunov, P. Umari, and R. M. Wentzcovitch, QUANTUM ESPRESSO: a modular and open-source software project for quantum simulations of materials, J. Phys.: Condens. Matter **21**, 395502 (2009).

[53] D. Vanderbilt, Soft self-consistent pseudopotentials in a generalized eigenvalue formalism, Phys. Rev. B **41**, 7892(R) (1990).

[54] A. M. Rappe, K. M. Rabe, E. Kaxiras, and J. D. Joannopoulos, Optimized pseudopotentials, Phys. Rev. B **41**, 1227(R) (1990).

[55] L. Kleinman and D. M. Bylander, Efficacious Form for Model Pseudopotentials, Phys. Rev. Lett. **48**, 1425 (1982).

[56] J. P. Perdew, K. Burke, and M. Ernzerhof, Generalized Gradient Approximation Made Simple, Phys. Rev. Lett **77**, 3865 (1996); **78**, 1396(E) (1997).

[57] H. J. Monkhorst and J. D. Pack, Special points for Brillouin-zone integrations, Phys. Rev. B **13**, 5188 (1976).

[58] C. G. Broyden, The convergence of a class of double-rank minimization algorithms 1. General considerations, IMA Jour. of Appl. Math. **6**, 76 (1970).

[59] Few preliminary results where reported in the proceeding of EMRS-2017 fall meeting, Ref. [43].

[60] R. Skomski, *Simple Models of Magnetism* (Oxford University Press, Oxford, 2008).

[61] M. Lindgren and I. Pan, Oxygen vacancy formation, mobility, and hydrogen pick-up during oxidation of zirconium by water, Oxid. Met. **87**, 355 (2017).